Received 21 October 2022; revised 18 November 2022; accepted 21 November 2022. Date of publication 24 November 2022; date of current version 2 December 2022.

Digital Object Identifier 10.1109/OJCOMS.2022.3224562

On the Performance of RIS-Assisted Communications With Direct Link Over κ-μ Shadowed Fading

ASHRAF AL-RIMAWI [1] (Member, IEEE), AND ARAFAT AL-DWEIK [2,3] (Senior Member, IEEE)

[1]Department of Electrical and Computer Engineering, Birzeit University, Birzeit P627, Palestine

[2]Center for Cyber Physical Systems, Khalifa University, Abu Dhabi, UAE

[3]Department of Electrical and Computer Engineering, Western University, London, ON N6A 3K7, Canada

CORRESPONDING AUTHOR: A. AL-DWEIK (e-mail: dweik@fulbrightmail.org)

This work was supported by the Khalifa University Competitive Internal Research Award under Grant CIRA-2020-056.

ABSTRACT In reconfigurable intelligent surface (RIS)-assisted communications, the signal-to-noise ratio (SNR) is improved by optimizing the reflecting elements' phases to make the reflected signals add coherently at the receiver. Nevertheless, the RIS cannot control the phase of the direct link if it exists. Although the RIS phase can still be controlled such that the direct and reflected signals add coherently, the SNR gain might be hindered. Therefore, this paper considers the performance analysis of such scenarios where a novel analytical framework is developed to evaluate the SNR, outage probability, and bit error rate (BER). To capture a broad range of fading conditions, the channels are modeled as independent but not identically distributed generalized κ-μ shadowed fading channels. The Laplace transform is used to derive an accurate approximation of the probability density function (PDF) and cumulative distribution function (CDF) of the instantaneous fading, which are used to derive the PDF and CDF of the instantaneous SNR. The paper also considers deriving the asymptotic PDF, CDF, moment generating function (MGF) of the SNR, as well as the outage probability and BER. The obtained results show that a strong direct link may limit the gain obtained using the RIS.

INDEX TERMS κ-μ shadowed fading, RIS, intelligent surfaces, diversity order, outage probability, MGF, BER, sixth generation (6G).

I. INTRODUCTION

THE DEMAND for mobile data access has been growing rapidly in the past few years, driven by a large number of new subscribers, high data rate applications, and emerging Internet of Things (IoT) applications, which require massive connectivity. Therefore, the limited capacity problem became prominent [1], [2]. According to Ericsson mobility report [3], mobile network data traffic grew 44% between 2020 and 2021, and reached 72 Exabyte per month generated by about 8 billion subscribers. As per Cisco report [4], 50% of all IoT networked devices in 2023 will be connected to cellular networks. Therefore, the wireless network is expected to support about 15 billion IoT devices in addition to 8 billion mobile users. Although the advancements achieved by fifth generation (5G) wireless networks are considered substantial as compared to the fourth generation (4G), 5G networks' capacity improvement is still way below the 1000× capacity increase specified by the International Mobile Telecommunications-2020 (IMT-2020) vision.

To resolve the limited capacity problem, extensive research efforts are being dedicated to designing efficient solutions. For example, spectral capacity solutions aim at introducing more spectrum by utilizing new frequency bands, particularly high frequencies such as millimeter waves (mmW). However, mmW poses several challenges [5] such as the poor propagation characteristics of mmW as compared to the classical sub-6 GHz spectrum. Moreover, in highly-dense urban areas, the high-rise buildings cause shadowing

TABLE 1. References which considered direct and indirect links. The abbreviations are defined as: outage probability (OP), coverage probability (CP), average error probability (AEP), energy efficiency (EE), spectral efficiency (SE), and ergodic capacity (EC).

Ref	Direct Link	Performance Metric	No. of Antennas	Approach for Analysis	Channel	Phase knowledge	Modulation Schemes
[11]	–	OP, AEP and EC	SISO	Gamma distribution	Rayleigh	Perfect	M-QAM
[21]	–	OP	SISO	Exact and bounds	Fox's H	Imperfect	-
[22]	–	OP	SISO	Bounds	Rayleigh	Imperfect	-
[23]	–	OP	SISO	Chernoff bounds	Rayleigh	Perfect	-
[24]	–	OP	SISO	CLT	Nakagami-$\bar{m}$	Perfect	MQAM
[25]	–	SE, EE and EC	SISO	CLT	Nakagami-$\bar{m}$	Perfect	MQAM
[26]	–	OP	SISO	K_G distribution	Rayleigh	Imperfect	-
[27]	–	OP, SE and EE	SISO	Gamma distribution	Nakagami-$\bar{m}$	Perfect	-
[28]	–	OP, and AEP	SISO	K-distribution	Rayleigh/Rician	Perfect	BPSK/QAM
[29]	–	OP, AEP and EC	SISO	CLT	Rayleigh	Perfect	BPSK, and M-QAM
[30]	–	OP, AEP and EC	MIMO	K_G distribution	Rayleigh	Perfect	DPSK
[30]	–	OP, and EC	SISO	Gamma distribution	Rayleigh	Perfect	–
[31]	–	AEP	SISO	Nakagami-$\bar{m}$	Arbitrary	Imperfect	BPSK
[32]	–	OP and EC	SISO	Gamma distribution	Arbitrary	Perfect	–
[24]	–	OP and EC	SISO	Fox H function	Arbitrary	Imperfect	–
[33]	–	EC	MIMO	CLT	Arbitrary	Imperfect	–
[34]	–	EC	MIMO	CLT	Rician	Perfect	–
[35]	–	AEP	SISO	CLT	Rayleigh	Perfect	MPSK/QAM
[47]	–	OP	SIMO	CLT	Rician	Imperfect	–
[48]	✓	EC	SISO	CLT	Rayleigh	Imperfect	–
[36]	✓	OP, and EC	SISO	CLT	Rayleigh	Imperfect	–
[37]	✓	OP, and EC	SISO	leveraging Theorem	Rayleigh, and Rician	perfect	–
[38]	✓	OP	SISO	Gamma Distribution	Nakagami-$\bar{m}$	Perfect	–
[39]	✓	SEP	SISO	Gamma Distribution	Nakagami-$\bar{m}$	perfect	BPSK, and 4QAM
[40]	✓	OP, and EC	SISO	CLT	Nakagami-$\bar{m}$	perfect	-
[41]	✓	OP, AEP and EC	SISO	Tight Approximation	Rician and K-distribution	Perfect	BPSK
[42]	✓	CP	SISO	CLT	Nakagami-$\bar{m}$	Perfect	–
[43]	✓	EC	SISO	CLT	Rayleigh	Perfect	–

and mostly block line-of-sight (LOS) connectivity, which makes it more challenging for high-frequency transmission. Consequently, RISs were introduced to control the wireless environment [6], [7], [8], [9], [10]. An RIS panel consists of two-dimensional meta-surfaces arrays in which each meta-surface element can independently change the phase-shift of the incident electromagnetic signal to create a preferable wireless environment [11]. RIS panels do not require high hardware complexity or cost overhead during their integration, while they can provide a substantial gain in terms of reliability and network capacity [12].

Due to the wide range of use cases and applications anticipated for 5G and 6G wireless networks, conventional channel models are unlikely to be sufficient to capture the propagation channels for such applications [13]. For example, future wireless networks are expected to operate at an extremely broad spectrum of carrier frequencies ranging from 0.5 to 100 GHz. Therefore, a highly dynamic channel model is required to model the buildings' penetration loss, atmospheric attenuation, and multipath reflections. Moreover, small-cell densification and the invasion of IoT have triggered the use of outdoor-indoor and indoor-outdoor channels, which cannot be captured by conventional channel models [14]. High bandwidth transmission also requires a flexible channel model to capture the propagation effects that the signal might go through. unmanned aerial vehicle (UAV) and flying networks is another emerging application that requires a nontraditional channel model [15].

In the literature, several composite channel models such as the $\overline{\kappa\text{-}\mu}$/inverse and η-$\bar{\mu}$/inverse gamma fading are used to capture the statistical behavior of the combined small-scale and large-scale fading in various propagation environments [16]. However, such models assume that the shadowing affects the scattered and dominant waves equally, and thus, such models are referred to as multiplicative shadow fading models [17], [18]. However, in practice, the shadowing often affects only the dominant components. Therefore, such a model is referred to as LOS shadow fading model [19], [20].

A. RELATED WORK

RIS has recently attracted extensive research efforts, particularly performance analysis. The performance analysis was obtained for various system and channel models using several performance metrics such as SNR, BER, symbol error rate (SER), outage probability and capacity. Based on the received signal arrival, the system model can be generally classified into two main categories, RIS without direct link [6], [11], [21], [22], [23], [24], [25], [26], [27], [28], [29], [30], [31], [32], [33], which is more common, and with direct link [34], [35], [36], [37], [38]. Table 1 shows the classification of selected recent articles based on their consideration of the direct link, system model, channel model, and performance metric.

1) RIS WITHOUT DIRECT LINK

In [6], [11], [21], [22], [23], [24], [25], [28], [29], [30], [31], [32], [33], the authors provide closed-form exact and approximations for several performance metrics through modeling the end-to-end RIS channel amplitude as Rayleigh [6], [30], Gamma [11], [26], [27], and Nakagami-$\bar{m}$ [28] distributions. Moreover, the channel [24], [25], [29] is based on Central Limit Theorem (CLT) which is not accurate for a small number of reflecting elements. In [24], a unified analytical framework is developed based on the Fox-H function, which is shown to be highly accurate even for a small number of reflecting elements, particularly for continuous phase shifts.

2) RIS WITH DIRECT LINK

The work on performance analysis of RIS with direct link that is considered in [35], [36], [37], [38], [39], [40], [41], [42], [43] is based on approximating the end-to-end SNR using various approximation methods such as the CLT. As shown in Table 1, the channel model in [35], [36], [37], [38], [42], [43] is considered as Nakagami-$\bar{m}$, Rician and Rayleigh fading. Waqar [41] considers the Rician and K-fading models. It is worth mentioning that the aforementioned fading models do not accurately capture the composite fading and shadowing that is usually experienced in practical channel models.

B. MOTIVATION AND CONTRIBUTION

As can be noted from the surveyed literature and references listed therein, most of the published research on RIS neglects the direct link between the base stations (BS) and user equipment (UE) based on the assumption that the direct link signal strength is much smaller than the reflected one. However, this may not be the case in practice because the direct link can be significant in some scenarios as compared to the RIS route due to the intrinsic product of the path loss [33], [44]. To this end, κ-μ shadowed distribution is widely used in literature for modeling composite fading/shadowing. It has a clear physical interpretation, good analytical properties and unifies popular fading models such as One-Side Gaussian, Rayleigh, Nakagami-$\bar{m}$, Rician, $\overline{\kappa}$-$\overline{\mu}$, and η-$\bar{\mu}$ fading channels as special cases as reported in [45] and [46, Table 1]. Based on the surveyed literature and the references listed therein, and to the best of the authors' knowledge, there is no published work that develops an analytical framework for studying RIS-assisted wireless communications systems with direct link in the generalized κ-μ shadowed fading channel. Most of the considered fading models in the literature such as the Rician, Nakagmai-$\bar{m}$ and Rayleigh are actually special cases of the fading model considered in this work. More specifically, the main contribution of this paper can be summarized as follows:

- Develops a new and generalized analytical framework model to evaluate the performance of the RIS-assisted wireless communications systems in the presence of a direct link between the BS and UE.
- Derives accurate closed-from expressions for the PDF, MGF, and CDF of the end-to-end SNR.
- Derives accurate closed-form approximations for the Outage Probability (Pout) and BER.
- Derives a new accurate closed-form expression for the asymptotic Pout and BER. Moreover, the system diversity order and coding gain are provided.
- The derived results are valid for an arbitrary number of reflecting elements, and various values of κ-μ shadowed parameters.
- Simulation results are provided to validate our analysis.

TABLE 2. List of functions, $a_p = a_1, \ldots, a_p$; $b_q = b_1, \ldots, b_q$.

Symbol	Function
$\mathbb{E}[\cdot]$	Statistical expectation
$\mathrm{Var}(\cdot)$	Statistical variance
$\Pr[\cdot]$	Probability operation
$\mathcal{L}[\cdot]$	Laplace transform
$\mathcal{L}^{-1}[\cdot]$	Inverse Laplace transform
$M_v(\cdot)$	Moment generating function
$f_X(\cdot)$	Probability density
$F_X(\cdot)$	Cumulative distribution function
$\Gamma(\cdot)$,	gamma [50, eq. (8.310)]
$\gamma(.,.)$	Lower incomplete gamma [50, eq. (8.350)]
$K_v(\cdot)$	Modified Bessel of order v [51, eq. (9.6.2)]
Φ_2	Bivariate confluent hypergeometric [52]
${}_1\tilde{F}_1(\cdot)$	Regularized hypergeometric function (HF)
${}_1F_1(.;.;.)$	Confluent HF [50, eq. (8.310)]
${}_pF_q(\mathbf{a}_p;\mathbf{b}_q;x)$	Generalized HF [50, eq. (9.14)]
$B(\cdot,\cdot)$	Beta [50, eq. (8.38)]

C. PAPER ORGANIZATION AND NOTATIONS

The remainder of this work is organized as follows. Section II presents the system and channel models, the PDF of the received signal power, the MGFs and CDF of the overall channel gain, and the PDF of the end-to-end SNR. Section III presents the performance evaluation in terms of outage and bit error probabilities. Section IV evaluates the numerical results for various system and channel scenarios, and discusses the main findings. Finally, Section V concludes the paper and Appendix presents the proof Proposition 2. The notations used throughout the paper are listed in Table 2.

II. SYSTEM AND CHANNEL MODELS

A. SYSTEM MODEL

The simplified system model is given in Fig. 1, where an RIS -assisted wireless communications network that includes a BS, RIS panel equipped with N reflecting elements, and K UEs. Each UE can access the RIS through an orthogonal multiple access protocol such as time division multiple access (TDMA). In this work, we consider that the UE can receive the transmitted signal through two different links, an indirect link through the RIS and a direct link from the BS. It is worth noting that using the term direct should not imply that the BS and UE have a LOS connectivity, it just indicates that the signal propagates from the BS to the UE without RIS assistance. Because the distance between the RIS panel, BS and UE is much larger than the distance between the reflecting elements within the RIS panel, then all RIS elements are

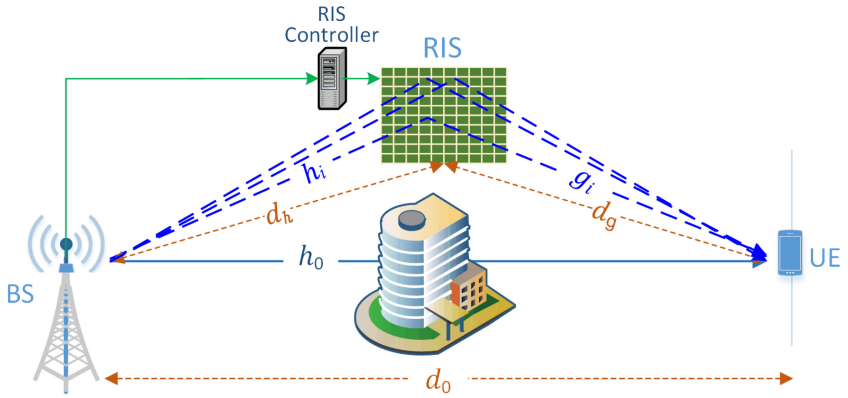

FIGURE 1. RIS system model with reflected and direct links. The direct link distance and channel gain are denoted as d_0 and h_0, respectively. The BS-RIS link distance with respect to the ith reflecting element are d_i and h_i, $i > 0$. Similarly, the RIS-UE link distance and channel gain are d_g and g_i.

assumed to be at the same distance from the BS and UE. Therefore, the distances from BS to UE, BS to RIS, and RIS to UE are respectively denoted as d_0, d_h, and d_g. Practically speaking, the width/length of the RIS elements as well as the spacing between adjacent elements can be smaller than half the wavelength [52]. Therefore, the channels between adjacent elements become spatially correlated [53], [54], [55]. However, most of the reported research considers that the channels for all RIS elements are independent and identically distributed (i.i.d.) [12], [36], [38], [56], [57], [58]. Such an assumption can be validated by noting that the elements' size is typically about $0.5\lambda_F \times 0.5\lambda_F$ [52], where λ_F is the carrier frequency wavelength. Therefore, the distance between the centers of adjacent elements is slightly more than $\lambda_F/2$. Moreover, the separation between an element and the next adjacent element becomes more than half the wavelength. Which significantly limits the number of correlated elements in the RIS panel. The i.i.d. assumption also enables mathematical tractability, particularly when a generalized channel model is considered, which is the case in this work. The channel gains between the BS and RIS, RIS and UE are denoted as h_i, and g_i, respectively, $i = 1, 2, \ldots, N$. The channel gain between the BS and UE is denoted as h_0. The channel state information (CSI) of each UE is communicated to the BS by means of channel reciprocity algorithms, or via a feedback channel. The BS controls the phase of each RIS element through a programmable controller attached to the RIS panel through a feedback channel [6], [59], [60].

For mathematical tractability, we consider that the BS and UE are equipped with a single antenna [61], [62], [63]. Therefore, the received signal at any UE can be expressed as

$$Y = Y_D + Y_R + n \tag{1}$$

where Y_D is the signal received through the direct link, Y_R is the signal received through the RIS, and $n \sim \mathcal{CN}(0, N_0)$ is the additive white Gaussian noise (AWGN). The direct signal can be written as [42]

$$Y_D = \sqrt{P} d_0^{-\frac{\alpha_D}{2}} \zeta^{\frac{1}{2}} |h_0| \mathrm{e}^{-j\theta_0} s \tag{2}$$

where P is the transmitted power, $\zeta = (\frac{c}{4\pi f_c})^2$ denotes the average channel gain at a reference distance of 1 m based on the free space path-loss model, c is the speed of light, f_c is the carrier frequency, s is the transmitted information symbol, $|h_0|$ and θ_0 are the magnitude and phase of the channel from the BS to UE, and α_D is the pathloss exponent at direct link.

Similarity, Y_R denotes the received signal at UE through the RIS link, which can be written as,

$$Y_R = \sqrt{P}\zeta d_h^{-\frac{\alpha_R}{2}} d_g^{-\frac{\alpha_R}{2}} s \sum_{i=1}^{N} |h_i| \mathrm{e}^{-j\theta_i} v_i \mathrm{e}^{j\Psi_i} |g_i| \mathrm{e}^{-j\phi_i} \tag{3}$$

where $|h_i|$ and θ_i denote the magnitude and phase of h_i, respectively, while, $|g_i|$ and ϕ_i are the magnitude and phase of g_i the UE, respectively. The ith RIS element gain and phase are v_i and Ψ_i. Without loss of generality, we consider that $v_i = 1$ [11], [61], [62], [63], [64]. Therefore, we can write

$$Y_R + Y_D = \left(\zeta d_h^{-\frac{\alpha_R}{2}} d_g^{-\frac{\alpha_R}{2}} \sum_{i=1}^{N} |h_i||g_i| \mathrm{e}^{-j(\theta_i+\phi_i-\Psi_i-\theta_0)} + d_0^{-\frac{\alpha_D}{2}} \zeta^{\frac{1}{2}} |h_0| \right) s\sqrt{P} \mathrm{e}^{-j\theta_0}. \tag{4}$$

If we choose the phases such that [64], [65], [66], [67],

$$\theta_i + \phi_i - \Psi_i - \theta_0 = 0 \tag{5}$$

then

$$\begin{aligned} Y_R + Y_D &= \sqrt{P}\mathrm{e}^{-j\theta_0} \left(\frac{\zeta}{d_h^{\frac{\alpha_R}{2}} d_g^{\frac{\alpha_R}{2}}} \sum_{i=1}^{N} |h_i||g_i| + \frac{\sqrt{\zeta}}{d_0^{\frac{\alpha_D}{2}}} |h_0| \right) s \\ &= (H_R + H_D)\mathrm{e}^{-j\theta_0} s. \end{aligned} \tag{6}$$

Consequently, the overall channel gain can be expressed as

$$V = H_D + H_R. \tag{7}$$

Therefore, combining the direct and reflected signals coherently at the UE is still possible using the RIS even though the direct link phase cannot be controlled. The power of the combined signals in this case is $|V|^2$ and the PDF of the SNR is given in (38).

TABLE 3. Parameter values for the envelope κ-μ shadowed distribution [68].

Case $\mu > \omega$		Case $\mu \leq \omega$
$M = \mu$		$M = \omega - \mu$
$C_i = \begin{cases} 0 & i = 0 \\ (-1)^{\omega} \binom{\omega+i-2}{i-1} \left[\frac{\omega}{\mu k+\omega}\right]^{\omega} \left[\frac{\mu k}{\mu k+\omega}\right]^{-\omega-i+1} & 0 < i \leq \mu - \omega \\ (-1)^{i-\mu+\omega-1} \binom{i-2}{i-\mu+\omega-1} \left[\frac{\omega}{\mu k+\omega}\right]^{i-\mu+\omega-1} \left[\frac{\mu k}{\mu k+\omega}\right]^{1-i} & \mu - \omega < i \leq \mu \end{cases}$		$\binom{\omega-\mu}{i} \left[\frac{\omega}{\mu k+\omega}\right]^{i} \left[\frac{\mu k}{\mu k+\omega}\right]^{\omega-\mu-i}$
$m_i = \begin{cases} \mu - \omega - i + 1 & 0 \leq i \leq \mu - \omega \\ \mu - i + 1 & \mu - \omega \leq i \leq \mu \end{cases}$		$m_i = \omega - i$
$\Omega_i = \begin{cases} \frac{1}{\mu(1+k)} & 0 \leq i \leq \mu - \omega \\ \frac{\mu k+\omega}{\omega} \frac{1}{\mu(1+k)} & \mu - \omega \leq i \leq \mu \end{cases}$		$\Omega_i = \frac{\mu k+\omega}{\omega} \frac{1}{\mu(1+k)}$

B. CHANNEL MODEL

The κ-μ shadowed model is denoted as κ-μ, is a generalized distribution that plays an essential role in modeling fading for LOS scenarios. The κ-μ shadowed model has an additional parameter ω, as compared to $\overline{\kappa\text{-}\mu}$ model, which is related to shadowing. Consequently, it has a clear physical interpretation, flexible analytical properties, and can represent common fading models such as One-Side Gaussian, Rayleigh, Nakagami- $\bar{m}$, Rician, $\overline{\kappa\text{-}\mu}$, and η-$\bar{\mu}$ fading channels as special cases [45], [46, Table 1]. In addition, it can be used in several real-world applications [19], [69], [70], [71]. By limiting the fading parameters μ and ω to integer values, minor differences are obtained in practice when fitting field measurements to the κ-μ, while it will make the mathematical analysis more tractable and may lead to efficient closed-form expressions [68]. More specifically, the measurements' results in [68, Figs. 6, 7] confirm that limiting the values of ω and μ to integer values would produce negligible differences in the CDF of the channel, particularly for $\omega \geq 2$. For RIS applications, the value of ω is generally larger than 2 because the RIS panel is intentionally located to have strong links with both the transmitter and receiver. For the direct link, the value of ω could be less than 2, however, the performance is generally dominated by the RIS link. Fig. 2 shows the PDF $f_V(v)$ for various integer and noninteger parameters where it is clearly shown that the integer assumption has an insignificant effect on the PDF. In this work, we consider that all channel gains follow the κ-μ shadowed with integer μ and ω parameters. Therefore, the PDF of the envelope can be obtained from the PDF of the power [68, eq. (12)] using transformation between two random variables (RVs). Consequently, the κ-μ shadowed envelope PDF and CDF can be respectively expressed as

$$f_X(x) = \sum_{i=0}^{M} \frac{2C_i x^{2m_i-1}}{\Gamma(m_i)\Omega_i^{m_i}} \mathrm{e}^{-\frac{x^2}{\Omega_i}} \tag{8}$$

and

$$F_X(x) = 1 - \sum_{i=0}^{M} C_i \mathrm{e}^{-\frac{x}{\Omega_i}} \sum_{k=0}^{m_i-1} \frac{1}{k!} \left(\frac{x}{\Omega_i}\right)^k \tag{9}$$

where M, C_i, m_i, and Ω_i are given in Table 3.

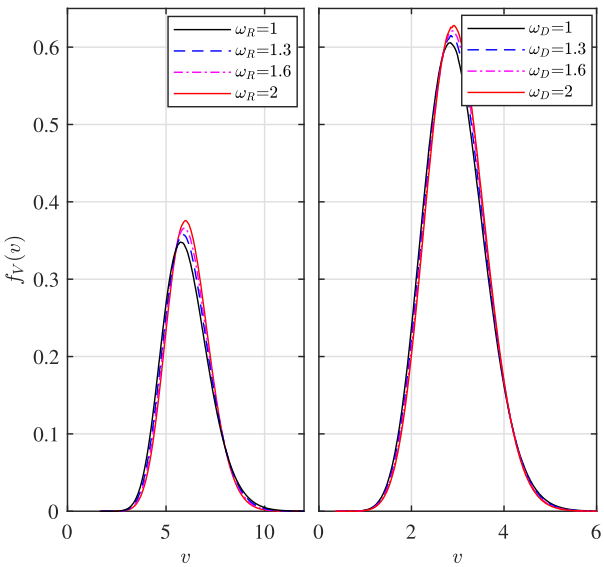

FIGURE 2. (a) Evolution of the simulation PDF $f_V(v)$ for different values of ω_D and fixed $\omega_R = 5$. Parameter values $N = 20$, $\mu_R = \mu_D = 2$ and $\omega_R = 5$, and $\kappa_D = \kappa_R = 1$. (b) Evolution of the simulation PDF $f_V(v)$ for different values of ω_R and fixed $\omega_D = 5$. Parameter values $N = 20$, $\mu_R = \mu_D = 2$ and $\omega_D = 5$, and $\kappa_D = \kappa_R = 1$.

C. PDF OF THE RECEIVED SIGNAL POWER

As can be noted from (6) and (7), the received signal power depends on V, and thus, its PDF should be derived. Towards this goal, define $|h_i||g_i| \triangleq \bar{Z}_i$, and for notational simplicity, we drop the reflector index i unless it is necessary to include. Therefore, the PDF of $\bar{Z}$ can be evaluated as [72],

$$f_{\bar{Z}_i}(z) = \int_0^{\infty} \frac{1}{x} f_h(x) f_g\left(\frac{z}{x}\right) dx. \tag{10}$$

By substituting the PDFs $|h| \sim \kappa\mu(M_1, C_i, m_i, \Omega_i)$, and $|g| \sim \kappa\mu(M_2, C_j, m_j, \Omega_j)$ expressed in (8), into (10), and using the identity [49, eq. (3.471.9)]

$$\int_0^{\infty} x^{\nu-1} \mathrm{e}^{\frac{\beta}{x}-\gamma x} dx = 2\left(\frac{\beta}{\gamma}\right)^{\frac{\nu}{2}} K_{\nu}\left(2\sqrt{\beta\gamma}\right) \tag{11}$$

we obtain,

$$f_{\bar{Z}_i}(z) = \sum_{i=0}^{M_1} \sum_{j=0}^{M_2} \frac{4C_i C_j}{\Gamma(m_i)\Gamma(m_j)} \frac{1}{\Omega_i^{\frac{m_i+m_j}{2}}}$$

$$\times \frac{1}{\Omega_i^{\frac{m_i+m_j}{2}}} z^{m_i+m_j-1} K_{m_i-m_j}\left(\frac{2z}{\sqrt{\Omega_i\Omega_j}}\right). \quad (12)$$

Moreover, the mean and variance of $\bar{Z}_i$ are respectively given by,

$$\mathbb{E}\big[\bar{Z}_i\big] \triangleq \mu_{\bar{Z}_i} = \sum_{j=0}^{M_1}\sum_{k=0}^{M_2} \frac{C_iC_j}{\Gamma(m_i)\Gamma(m_j)}(\Omega_i\Omega_j)^{\frac{1}{2}} \times \left[\Gamma\left(\frac{1}{2}(m_i+m_j+1)\right)\right]^2 \quad (13)$$

and

$$\mathrm{Var}\big[\bar{Z}_i\big] \triangleq \sigma^2_{\bar{Z}_i} = \mathbb{E}\big[\bar{Z}_i^2\big] - \big(\mathbb{E}\big[\bar{Z}_i\big]\big)^2 \quad (14)$$

where

$$\mathbb{E}\Big[\bar{Z}_i^2\Big] \triangleq \sum_{j=0}^{M_1}\sum_{k=0}^{M_2} \frac{C_iC_j}{\Gamma(m_i)\Gamma(m_j)}(\Omega_i\Omega_j) \times \left[\Gamma\left(\frac{1}{2}(m_i+m_j+2)\right)\right]^2. \quad (15)$$

In the special case where all the links are identical, i.e., $M_1 = M_2 = M$, $\Omega_j = \Omega_i = \Omega_l$, and $C_j = C_i = C_l$), then

$$f_{\bar{Z}_i}(z) = \sum_{l=0}^{M} \frac{4C_l^2}{[\Gamma(m_l)]^2}\frac{1}{\Omega_l^{2m_l}} z^{2m_l-1} K_0\left(\frac{2z}{\Omega_l}\right) \quad (16)$$

$$\mathbb{E}\big[\bar{Z}_i\big] \triangleq \mu_{\bar{Z}_i} = \sum_{l=0}^{M} \frac{\Omega_l C_l^2}{[\Gamma(m_l)]^2}\left[\Gamma\left(m_l+\frac{1}{2}\right)\right]^2 \quad (17)$$

and

$$\mathbb{E}\Big[\bar{Z}_i^2\Big] \triangleq \textstyle\sum_{l=0}^{M} \frac{\Omega_l^2 C_l^2}{[\Gamma(m_l)]^2}[\Gamma(m_l+1)]^2. \quad (18)$$

However, using the exact PDF $Z = \sum_{i=1}^{N} \bar{Z}_i$ and the moments of Z will lead to computationally complex and intractable analysis. Therefore, we use the approximation in [30] to simplify $f_Z(z)$ by using the gamma distribution,

$$f_Z(z) = \frac{z^{a-1}}{b^a\Gamma(a)}\exp\left(-\frac{z}{b}\right) \quad (19)$$

and

$$F_Z(z) = \frac{\gamma\left(a, \frac{z}{b}\right)}{\Gamma(a)} \quad (20)$$

where $a = \frac{\mu_Z^2}{\sigma_Z^2}$, $b = \frac{\sigma_Z^2}{\mu_Z}$, $\mu_Z = \sum_{i=1}^{N}\mu_{\bar{Z}_i}$ and $\sigma_Z^2 = \sum_{i=1}^{N}\sigma^2_{\bar{Z}_i}$. In case of i.i.d. channel gains, $\mu_Z = N\mu_{\bar{Z}_i}$ and $\sigma_Z^2 = N\sigma^2_{\bar{Z}_i}$. The expression in (19) will be used to attain simple and tractable expressions.

Proposition 1: Suppose that Z has gamma distribution with shape parameter $a \in (0, \infty)$ and scale parameter $b \in (0, \infty)$. For large values of N, the distribution of the RV Z converges to normal distribution such that

$$\acute{Z} = \frac{Z - ab}{\sqrt{ab}}. \quad (21)$$

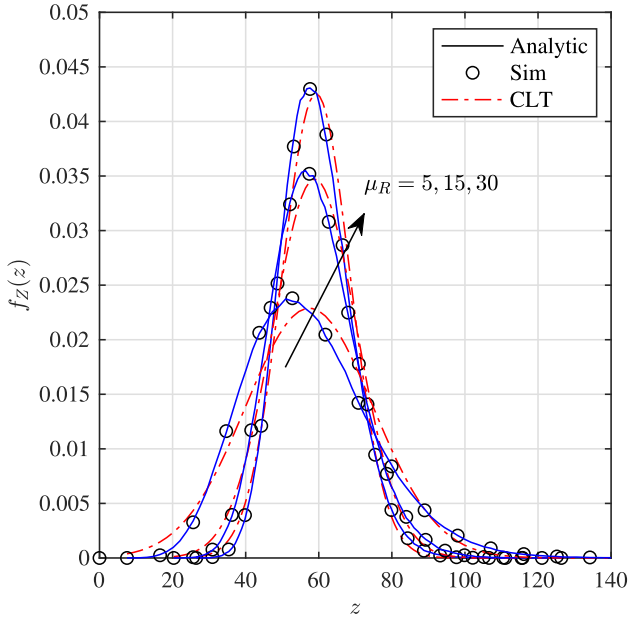

FIGURE 3. Comparison of the analytical PDF $f_Z(z)$ with CLT and Monte Carlo Simulations for different fading parameter μ_R: $N = 60$, $\kappa_R = 5$, and $\omega_R = 10$.

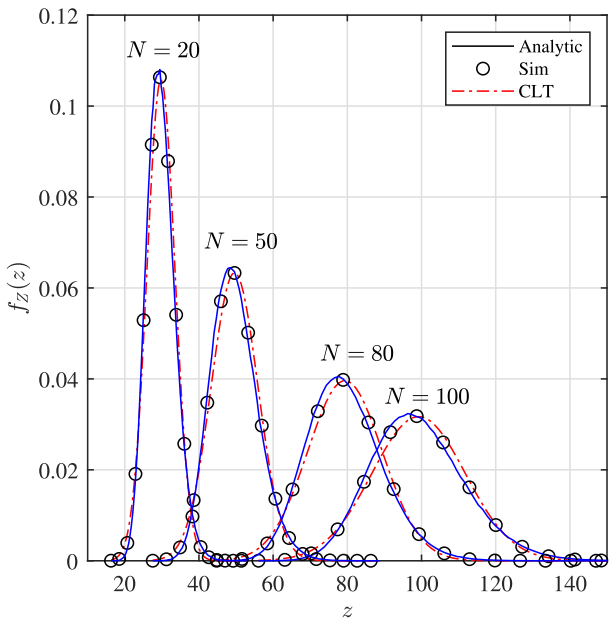

FIGURE 4. Comparison of the analytical PDF $f_Z(z)$ with CLT and Monte Carlo Simulations for different values of N: $\mu_R = 30$, $\kappa_R = 5$, and $\omega_R = 10$.

Figs. 3 and 4 illustrate the comparison between the PDF of the indirect link expressed in (19) with CLT method and Monte Carlo simulations. It can be noted that the PDF of the proposed approximation is more accurate than that based on the CLT regardless of the values of μ_R parameter and the number of reflecting elements N. In addition, in Fig. 4, PDF $f_Z(z)$ is evaluated for fixed and equal fading parameters where $N \in \{20, 50, 80, 100\}$. As the figure shows, the analytical and simulation results match perfectly, which confirms the accuracy of the derived expressions. Moreover, it

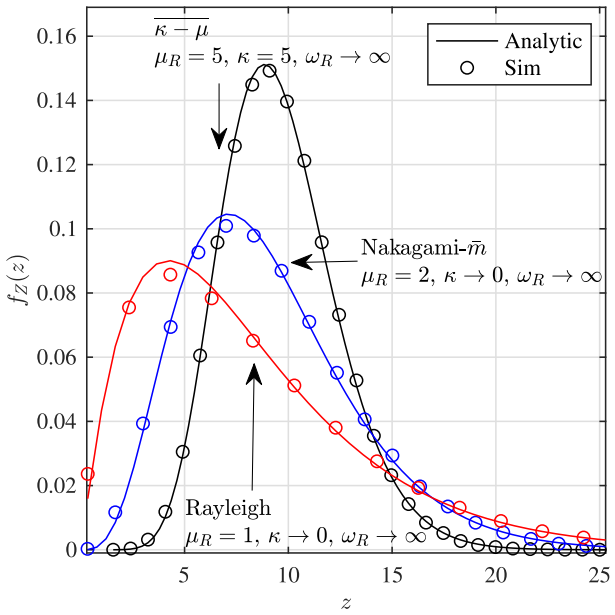

FIGURE 5. The PDF $f_Z(z)$ for different fading models as special cases of κ-μ shadowed distribution for $N = 10$.

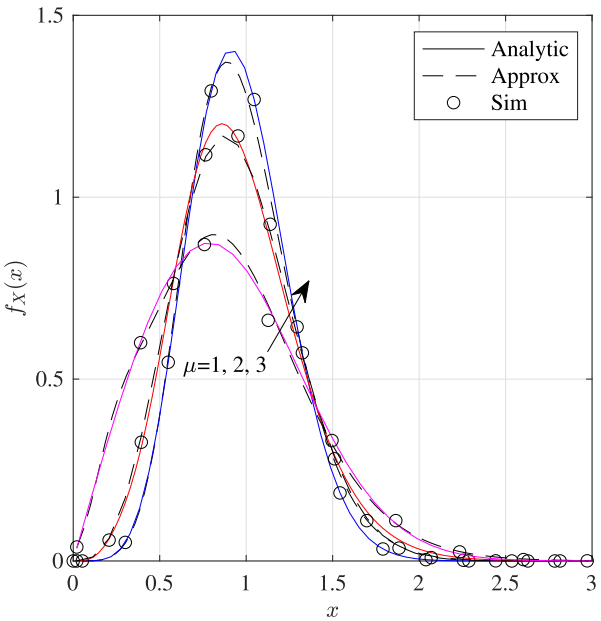

FIGURE 6. The exact (8), simulation, and approximated (24) PDF $f_X(x)$ for $\omega = 1$, and $\kappa = 1$ for different values of fading parameter μ.

can be noted that increasing N can significantly improve the fading conditions.

Fig. 5 demonstrates the effectiveness and validity of the derived PDFs by comparing the generalized theoretical expression of the PDF in (19) to Monte Carlo simulation. The values of μ, κ and ω of the individual PDFs are selected to correspond to some of the widely used PDFs, while N is fixed at 10. As the figure shows, the theoretical expression perfectly matches the simulation results for all considered scenarios. Moreover, the generalized distribution model can be used to represent the widely known fading distributions such as the Rayleigh, Nakagami-$\bar{m}$, and $\overline{\kappa\text{-}\mu}$.

By applying the transformation method between two random variables in (6) (i.e., $H_R = L_R Z$), the PDF and CDF of H_R can be given by

$$f_{H_R}(h_R) = \frac{(h_R)^{a-1}}{(L_R b)^a \Gamma(a)} \exp\left(-\frac{h_R}{L_R b}\right) \tag{22}$$

and

$$F_{H_R}(h_R) = \frac{\gamma\left(a, \frac{h_R}{L_R b}\right)}{\Gamma(a)} \tag{23}$$

where $L_R = \sqrt{P}\zeta d_h^{-\frac{\alpha_R}{2}} d_g^{-\frac{\alpha_R}{2}}$.

The PDF and CDF of H_D, i.e., $H_D = L_D|h_0|$, can be derived following the same approach used to derive $F_{H_R}(h_R)$, however, the PDF in (8) typically leads to significant computational complexity when $F_{H_R}(h_R)$ and $F_{H_D}(h_D)$ are convolved to compute $f_V(v)$. Consequently, we propose the following accurate approximation.

Proposition 2: Using Laplace approach, $f_X(x)$ in (8) can be approximated as

$$f_X(x) = \sum_{q=0}^{M} \sum_{\nu=1}^{5} \frac{\sqrt{\pi} C_q}{\Gamma(m_q) \Omega_q^{m_q - \frac{1}{2}}} \frac{\Lambda_2! a_\nu}{(\nu-1)! \Delta^\nu} \times \frac{1}{\Gamma(\Lambda_1)} x^{\Lambda_2} \exp\left(-\frac{x}{\Delta}\right) \tag{24}$$

where $\Lambda_1 = 2m_q + \nu - 1$, $\Lambda_2 = \Lambda_1 - 1$, $a_1 = 0.25482959$, $a_2 = -0.284496736$, $a_3 = 1.421413741$, $a_4 = -1.453152027$, $a_5 = 1.061405429$, $\Delta = \frac{p}{2}\sqrt{\Omega_i}$, and $p = 0.3275911$.

Proof: The proof is given in the Appendix. ■

Fig. 6 shows the PDF derived in (24) and evaluates its accuracy by comparing it with exact PDF in (8). The figure shows a close match between the exact and approximated PDFs for a wide range of x. However, a slight deviation is observed in the PDF tail region when $1.48 \lesssim x \lesssim 2$, and close to the peak of the PDFs. Such deviation is insignificant because it is generally small and appears only for a narrow range of values. By applying the Kullback–Leibler divergence test numerically over 300 samples we obtain a divergence factor of -8.1×10^{-2} for $\mu = 3$, and -1.9×10^{-2} for $\mu = 2$, which confirms the accuracy of the approximation.

Following the same approach used to derive $F_{H_R}(h_R)$, and using the approximated PDF in (24) gives

$$f_{H_D}(h_D) = \sum_{q=0}^{M_3} \sum_{\nu=1}^{5} \mathcal{G}_{q,\nu} \frac{1}{\Gamma(\Lambda_1)} h_D^{\Lambda_2} \mathrm{e}^{-\frac{h_D}{\Delta L_D}} \tag{25}$$

and

$$F_{H_D}(h_D) = \sum_{q=0}^{M_3}\sum_{v=1}^{5} \frac{\sqrt{\pi}C_q\Lambda_2!}{(v-1)!\Gamma(m_q)}\left(\frac{\Delta^2}{\Omega_q}\right)^{m_q-\frac{1}{2}} a_v \times \frac{1}{\Gamma(\Lambda_1)}\gamma\left(\Lambda_1, \frac{h_D}{\Delta L_D}\right) \quad (26)$$

respectively, where $L_D = \sqrt{P}d_0^{-\frac{\alpha_D}{2}}\zeta^{\frac{1}{2}}$, and

$$\mathcal{G}_{q,v} = \frac{\sqrt{\pi}C_q}{\Gamma(m_q)\left(L_D^2\Omega_q\right)^{m_q-\frac{1}{2}}}\frac{a_v\Lambda_2!}{(v-1)!(\Delta L_D)^v}. \quad (27)$$

By noting the superposition of H_D and H_R in (7), then the PDF of V can be obtained by applying the convolution theorem to (22) and (25). Thus,

$$\begin{aligned} f_V(v) &= \int_{-\infty}^{\infty} f_{H_D}(u)f_{H_R}(v-u)du \\ &= \sum_{q=0}^{M_3}\sum_{v=1}^{5} \frac{\mathcal{G}_{q,v}}{\Gamma(\Lambda_1)(L_Rb)^a}e^{\frac{-v}{L_Rb}}\int_0^v \frac{u^{\Lambda_2}}{(v-u)^{1-a}}e^{\Lambda\Upsilon}du \\ &= \sum_{q=0}^{M_3}\sum_{v=1}^{5} \frac{\mathcal{G}_{q,v}\ v^{\Lambda-1}}{\Gamma(\Lambda)(L_Rb)^a}e^{\frac{-v}{L_Rb}}{}_1F_1(\Lambda_1, \Lambda; \Upsilon v) \end{aligned} \quad (28)$$

where $\Lambda = 2m_q + v + a - 1$, $\Upsilon = (\frac{1}{L_Rb} - \frac{1}{\Delta L_D})$.

D. MOMENT GENERATING FUNCTION OF V

By applying the Laplace transform to (28), we obtain the MGF of V,

$$\begin{aligned} M_V(s) &= \mathcal{L}\left[f_V(v); -\left(s+\frac{1}{L_Rb}\right)\right] \\ &= \sum_{q=0}^{M_3}\sum_{v=1}^{5} \frac{\mathcal{G}_{q,v}}{\Gamma(\Lambda)}\frac{1}{(L_Rb)^a}\mathcal{L}\left[v^{\Lambda-1}{}_1F_1(\Lambda_1, \Lambda; \Upsilon v)\right]. \end{aligned} \quad (29)$$

Using [73, eq. (4.23.1)],

$$\begin{aligned} &\mathcal{L}\left[v^{\Lambda-1}{}_1F_1\left(\Lambda_1, \Lambda; \left(\frac{1}{L_Rb} - \frac{1}{\Delta L_D}\right)v\right)\right] \\ &\quad = \Gamma(\Lambda)\left(s+\frac{1}{L_Rb}\right)^{-a}\left(s+\frac{1}{\Delta L_D}\right)^{-\Lambda_1}. \end{aligned} \quad (30)$$

Therefore (29) becomes

$$M_V(s) = \sum_{q=0}^{M_3}\sum_{v=1}^{5} \frac{\mathcal{G}_{q,v}}{(L_Rb)^a}\left(s+\frac{1}{L_Rb}\right)^{-a}\left(s+\frac{1}{\Delta L_D}\right)^{-\Lambda_1}. \quad (31)$$

E. THE CDF OF V

By noting that the MGF in (31) and $f_V(v)$ has the relation

$$f_V(v) = \mathcal{L}^{-1}[M_V(s); v] \quad (32)$$

then $F_V(v)$ can be obtained as

$$F_V(v) = \mathcal{L}^{-1}\left[\frac{M_V(s)}{s}; v\right]. \quad (33)$$

By substituting (31) in (33), we obtain

$$\begin{aligned} F_V(v) = \mathcal{L}^{-1}\left[\frac{M_V(s)}{s}\right] &\sum_{q=0}^{M_3}\sum_{v=1}^{5} \frac{\sqrt{\pi}C_q}{\Gamma(m_q)} \\ &\times \frac{1}{\left(L_D^2\Omega_q\right)^{m_q-\frac{1}{2}}}\frac{a_v\Lambda_2!}{(v-1)!(\Delta L_D)^v}\frac{1}{(L_Rb)^a} \\ &\times \mathcal{L}^{-1}\left[\frac{1}{s}\left(s+\frac{1}{L_Rb}\right)^{-a}\left(s+\frac{1}{\Delta L_D}\right)^{-\Lambda_1}\right]. \end{aligned} \quad (34)$$

Using [73, eq. (4.24.3)], the Laplace inverse can be evaluated as,

$$\begin{aligned} &\mathcal{L}^{-1}\left[\frac{1}{s}\left(s+\frac{1}{L_Rb}\right)^{-a}\left(s+\frac{1}{L_D\Delta}\right)^{-\Lambda_1}\right] \\ &\quad = \frac{v^{\Lambda}}{\Gamma(\Lambda+1)}\Phi_2\left(a, \Lambda_1, \Lambda+1; -\frac{1}{L_Rb}v, -\frac{1}{\Delta L_Dv}\right). \end{aligned} \quad (35)$$

Substituting (35) into (34) gives,

$$\begin{aligned} F_V(v) &= \mathcal{L}^{-1}\left[\frac{M_V(s)}{s}\right] \\ &= \sum_{q=0}^{M_3}\sum_{v=1}^{5} \mathcal{G}_{q,v}\frac{v^{\Lambda}(L_Rb)^{-a}}{\Gamma(\Lambda+1)} \\ &\quad \times \Phi_2\left(a, \Lambda_1, \Lambda+1; -\frac{1}{L_Rb}v, -\frac{1}{\Delta L_Dv}\right) \end{aligned} \quad (36)$$

where the function Φ_2 can be efficiently computed by means of an inverse Laplace transform [74].

F. END-TO-END SNR

The instantaneous end-to-end SNR at the UE can be expressed as

$$\gamma_Y = \frac{\mathcal{P}_s}{N_0}|V|^2 = |V|^2\bar{\gamma} \quad (37)$$

where $\mathcal{P}_s$ is the transmitted symbol power, N_0 is AWGN noise power spectral density, and $\bar{\gamma}$ is the average SNR. Therefore, the PDF, CDF and MGF of γ_Y are respectively given by,

$$\begin{aligned} f_{\gamma_Y}(\gamma) &= \frac{1}{2\sqrt{\bar{\gamma}\gamma}}\sum_{q=0}^{M_3}\sum_{v=1}^{5} \frac{\mathcal{G}_{q,v}}{\Gamma(\Lambda)(L_Rb)^a}\left(\frac{\gamma}{\bar{\gamma}}\right)^{\frac{\Lambda-1}{2}} \\ &\quad \times e^{\xi}F_1\left(\Lambda_1, \Lambda; \Upsilon\sqrt{\frac{\gamma}{\bar{\gamma}}}\right). \end{aligned} \quad (38)$$

$$\begin{aligned} F_{\gamma_Y}(\gamma) &= \mathcal{L}^{-1}\left[\frac{M_V(s)}{s}\right] \\ &= \sum_{q=0}^{M_3}\sum_{v=1}^{5} \frac{\mathcal{G}_{q,v}}{(L_Rb)^a\ \Gamma(\Lambda)}\left(\frac{\gamma}{\bar{\gamma}}\right)^{\frac{\Lambda}{2}} \\ &\quad \times \Phi_2(a, \Lambda_1, \Lambda+2; \xi, \chi) \end{aligned} \quad (39)$$

$$(40)$$

where $\xi = -\frac{1}{L_R b}\sqrt{\frac{\gamma}{\bar{\gamma}}}$ and $\chi = -\frac{1}{\Delta L_D}\sqrt{\frac{\gamma}{\bar{\gamma}}}$, and

$$\begin{aligned}\mathrm{M}_{\gamma_Y}(s) &= \mathcal{L}\left[f_V(v); -\left(s+\frac{1}{L_R b}\right)\right] \\ &= \sum_{q=0}^{M_3}\sum_{v=1}^{5}\frac{\mathcal{G}_{q,v}\bar{\gamma}^{\frac{-\Lambda}{2}}}{(L_R b)^a}\left(s-\frac{\xi}{\sqrt{\gamma}}\right)^{-a}\left(s-\frac{\chi}{\sqrt{\gamma}}\right)^{-\Lambda_1}.\end{aligned} \tag{41}$$

To obtain more insights about the system behavior, we derive the asymptotic PDF, CDF and MGF in the high SNR region, i.e., $\bar{\gamma} \to \infty$. For the PDF,

$$f_{\gamma_Y}(\gamma)\big|_{\bar{\gamma}\to\infty} \triangleq f^{\infty}_{\gamma_Y}(\gamma) \tag{42}$$

by noting that [75]

$$\lim_{\bar{\gamma}\to\infty} {}_1F_1\left(\Lambda_1, \Lambda; \Upsilon\sqrt{\frac{\gamma}{\bar{\gamma}}}\right)\mathrm{e}^{\xi} = 1 \tag{43}$$

then we obtain from (38),

$$f^{\infty}_{\gamma_Y}(\gamma) = \frac{1}{2\sqrt{\bar{\gamma}\gamma}}\sum_{q=0}^{M_3}\sum_{v=1}^{5}\frac{\mathcal{G}_{q,v}}{\Gamma(\Lambda)(L_R b)^a}\left(\frac{\gamma}{\bar{\gamma}}\right)^{\frac{\Lambda-1}{2}}. \tag{44}$$

Similarly,

$$F^{\infty}_{\gamma_Y}(\gamma) = \sum_{q=0}^{M_3}\sum_{v=1}^{5}\frac{\mathcal{G}_{q,v}}{(L_R b)^a}\frac{1}{\Gamma(2m_q+a)}\left(\frac{\gamma}{\bar{\gamma}}\right)^{\frac{\Lambda}{2}} \tag{45}$$

and

$$\begin{aligned}\mathrm{M}^{\infty}_{\gamma_Y}(s) &= \mathcal{L}\left[f_V(v); -\left(s+\frac{1}{L_R b}\right)\right] \\ &= \sum_{q=0}^{M_3}\sum_{v=1}^{5}\frac{\mathcal{G}_{q,v}}{(L_R b)^a}\left(\frac{1}{\bar{\gamma}s^2}\right)^{\frac{\Lambda}{2}}.\end{aligned} \tag{46}$$

In the case that the UE has multiple receiving antennas, i.e., the system has single-input multiple-output (SIMO) configuration, then similar to (6), the received signal at the r^{th} receiving antenna can be written as,

$$\begin{aligned}Y_{R_r} + Y_{D_r} &= \sqrt{P}\mathrm{e}^{-j\theta_{0,r}} \\ &\quad\times\left(\frac{\zeta}{d_h^{\frac{\alpha_R}{2}}d_g^{\frac{\alpha_R}{2}}}\sum_{i=1}^{N}|h_{i,r}||g_{i,r}| + \frac{\sqrt{\zeta}}{d_0^{\frac{\alpha_D}{2}}}|h_{0,r}|\right)s \\ &= \left(H_{R_r} + H_{D_r}\right)\mathrm{e}^{-j\theta_{0,r}}s \\ &= V_r\mathrm{e}^{-j\theta_{0,r}}s.\end{aligned} \tag{47}$$

After Maximal Ratio Combining (MRC), the overall instantaneous SNR at UE can be expressed as

$$\gamma_\Sigma = \sum_{r=1}^{\mathrm{L}}\gamma_{Y_r} \tag{48}$$

where L is the number of receiving antennas, and γ_{Y_r} is defined in (38). However, deriving the exact PDF of γ_Σ generally leads to computationally complex and intractable analysis, and will be considered in a dedicated work.

III. PERFORMANCE EVALUATION

A. OUTAGE PROBABILITY

The derived distributions can be used to compute the outage probability, which is defined as

$$\begin{aligned}P_{out} &= \Pr\left[\gamma_Y \le \gamma_{out}\right] \\ &= F_{\gamma_Y}(\gamma_{out})\end{aligned} \tag{49}$$

where γ_{out} is a predetermined SNR threshold. From (45), it can be concluded that P_{out} can be approximated as

$$P_{out} \approx (G_o)^{-G_d} \tag{50}$$

where G_o and G_d denote the coding gain and diversity order which are respectively given by

$$G_o = \left(\sum_{q=0}^{M_3}\sum_{v=1}^{5}\frac{\mathcal{G}_{q,v}}{(L_R b)^a}\frac{1}{\Gamma(2m_q+a)}\right)^{-w}\frac{\bar{\gamma}}{\gamma} \tag{51}$$

where $w = \frac{2}{\Lambda}$, and $G_d = \frac{1}{w}$.

B. BIT ERROR RATE (BER)

Based on the MGF expressed in (41), the BER can be expressed as,

$$P_B = \frac{a_m}{\pi}\int_0^{\frac{\pi}{2}}\mathrm{M}_{\gamma_Y}\left(\frac{b_m^2}{2\sin^2(\vartheta)}\right)d\vartheta \tag{52}$$

where a_m and b_m are parameters that depend on the modulation scheme. By substituting (53) in (52), the BER becomes

$$\begin{aligned}P_B = \sum_{q=0}^{M_3}\sum_{v=1}^{5}\frac{a_m\mathcal{G}_{q,v}}{\pi(L_R b)^a}\frac{1}{\bar{\gamma}^{\frac{\Lambda}{2}}}\int_0^{\frac{\pi}{2}}\left(\frac{b_m^2}{2\sin^2(\vartheta)}-\frac{\xi}{\sqrt{\gamma}}\right)^{-a} \\ \times\left(\frac{b_m^2}{2\sin^2(\vartheta)}-\frac{\chi}{\sqrt{\gamma}}\right)^{-\Lambda_1}\mathrm{d}\vartheta.\end{aligned} \tag{53}$$

By performing the change of variable $t = \cos^2(\vartheta)$, and after some algebraic manipulations, we obtain

$$\begin{aligned}P_B = \sum_{q=0}^{M_3}\sum_{v=1}^{5}\frac{a_m}{\pi}\frac{\mathcal{G}_{q,v}}{(L_R b)^a}\left(\frac{b_m^2}{2}-\frac{\xi}{\sqrt{\gamma}}\right)^{-a}\left(\frac{1}{\bar{\gamma}}\right)^{\frac{\Lambda}{2}} \\ \times\left(\frac{b_m^2}{2}-\frac{\chi}{\sqrt{\gamma}}\right)^{-\Lambda_1}\int_0^1 t^{-\frac{1}{2}}(1-t)^{\Lambda+\frac{1}{2}} \\ \times(1-u_1 t)^{-(a)}(1-u_2 t)^{-\Lambda_1}\mathrm{d}t\end{aligned} \tag{54}$$

with the help of [49, eq. (3.211)]

$$\begin{aligned}&\int_0^1 t^{\lambda_1-1}(1-t)^{\mu_1-1}(1-u_1 t)^{-\varrho}(1-u_2 t)^{-\varsigma}\mathrm{d}t \\ &= \mathrm{B}(\mu_1,\lambda_1)F_1(\lambda_1,\varrho,\varsigma,\lambda_1+\mu_1;u_1,u_2)\end{aligned} \tag{55}$$

TABLE 4. Simulation parameters.

Parameters	Value
System Bandwidth (BW)	1 MHz
Power of AWGN (N_0)	-114 dB$_\text{m}$
Distance between BS and UE (d_0)	1000 m
Distance between BS and RIS (d_h)	1000 m
The distance between BS and RIS (d_g)	1000 m
Power attenuation at reference (1 m)	-30 dB$_\text{m}$
Transmitted Power (P)	1 W
Path loss exponent at all links	3.0
Target Threshold SNR γ_{out}	0 dB
Monte Carlo runs	10^4

then (54) becomes

$$P_B = \sum_{q=0}^{M_3}\sum_{\nu=1}^{5}\frac{a_m}{4\pi}\frac{\mathcal{G}_{q,\nu}}{(L_R b)^a}\frac{1}{\bar{\gamma}^{\frac{\Lambda}{2}}}\left(1-\frac{b_m^2\sqrt{\bar{\gamma}}}{2\xi}\right)^{-a} \times\left(1-\frac{b_m^2\sqrt{\bar{\gamma}}}{2\chi}\right)^{-\Lambda_1}\mathrm{B}\left(\Lambda+\frac{1}{2},\frac{1}{2}\right) \times F_1\left(\frac{1}{2},a,\Lambda_1,\Lambda+1;u_1,u_2\right) \tag{56}$$

where the values of u_1, and u_2 are respectively given by

$$u_1 = \frac{2}{1+2b_m^2 L_R b\sqrt{\bar{\gamma}}} \tag{57}$$

and

$$u_2 = \frac{2}{1+2b_m^2 \Delta L_D\sqrt{\bar{\gamma}}}. \tag{58}$$

For the asymptotic case where $\bar{\gamma}\to\infty$, we obtain

$$P_B^{\infty} = \sum_{q=0}^{M_3}\sum_{\nu=1}^{5}\frac{a_m}{4\sqrt{\pi}}\mathcal{G}_{q,\nu}\mathrm{B}\left(\Lambda+\frac{1}{2},\frac{1}{2}\right) \times\left(-\frac{2\xi}{b_m^2\sqrt{\bar{\gamma}}}\right)^{a}\left(-\frac{2\chi}{b_m^2\sqrt{\bar{\gamma}}}\right)^{\Lambda_1} \tag{59}$$

where the asymptotic BER can also be expressed in terms of coding G_p and diversity gain G_d, i.e., $P_B \approx (G_p\bar{\gamma})^{-G_d}$ [76, eq. (1)]

$$G_p = \left(\sum_{q=0}^{M_3}\sum_{\nu=1}^{5}\frac{a_m}{4\sqrt{\pi}}\mathcal{G}_{q,\nu}\mathrm{B}\left(\Lambda+\frac{1}{2},\frac{1}{2}\right)\left(\frac{2}{b_m^2}\right)^{\Lambda}\right)^{-w} \times\left(\left(\frac{1}{L_R b}\right)^{2a}\left(\frac{1}{\Delta L_D}\right)^{\Lambda_1}\right)^{-w} \tag{60}$$

and

$$G_d = \frac{1}{w}. \tag{61}$$

IV. NUMERICAL RESULTS

This section presents the theoretical and Monte Carlo simulation results for various cases of interest. The main simulation parameters are given in Table 4, unless specified otherwise. The results are obtained for various system and channel conditions. In particular, $\omega_{\{\cdot\}}$ specifies the level of fluctuation due to shadowing in the dominant component where low values of $\omega_{\{\cdot\}}$ indicate severe shadowing. Similarly, $\mu_{\{\cdot\}}$ of indicate the number of multipath clusters, and hence, increasing $\mu_{\{\cdot\}}$ can enhance the channel quality and improve the performance. The parameter $\kappa_{\{\cdot\}}$ is the ratio between the total power of the dominant components and the total power of the scattered waves. Large $\kappa_{\{\cdot\}}$ values indicate that the dominate component has more power than the scattered waves, and thus, the channel quality is better.

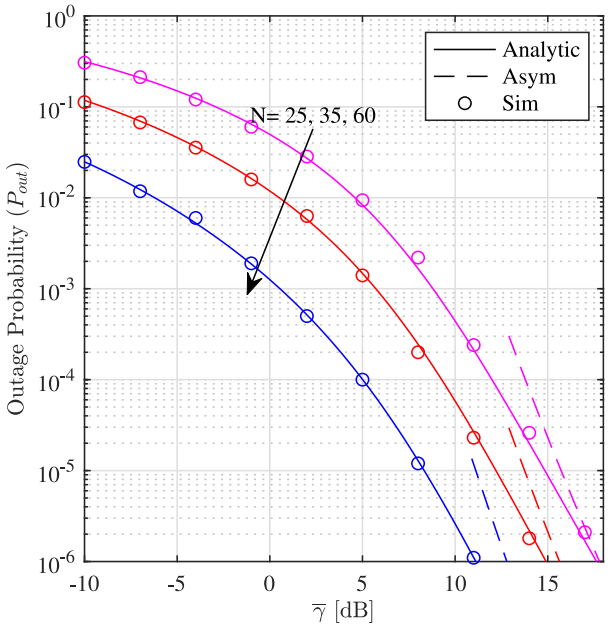

FIGURE 7. Outage probability versus $\bar{\gamma}$ for $N = 25, 35, 60$, $\omega_R = \omega_D = 5$, $\mu_R = 3$, $\mu_D = 2$, $\kappa_R = \kappa_D = 1$, $\gamma_{out} = 20$ dB.

Fig. 7 compares the analytical, asymptotic, and simulated outage probability versus SNR using various numbers of reflecting elements $N \in \{25, 35, 60\}$. As can be noted from the figure, the analytical and simulation results match very well for all the considered scenarios. It can be also observed that at high SNRs, the asymptotic and exact results converge. The improvement gained by increasing the number of reflectors increases non-linearly versus N. For example, increasing the number of reflectors from 25 to 35 reduced the SNR required to achieve P_{out} of 10^{-4} from 12 dB to 9 dB, i.e., the gain is about 3 dB while increasing N from 35 to 60 reflectors offers 4 dB gain. Therefore, the gain that can be achieved by increasing the number of reflectors decreases when the initial number of reflectors is small.

Fig. 8, Fig. 9 and Table 5 evaluate the impact of the various system and channel conditions on the outage and BER performance. As can be noted from Fig. 8, P_{out} is significantly dominated by the strength and quality of the direct path that is indicated by μ_D and the number of reflecting elements N in which increasing the values of μ and N can reduce P_{out}.

Table 5 highlight the influence of the shadowing parameter of the direct path ω_D between BS and UE for different

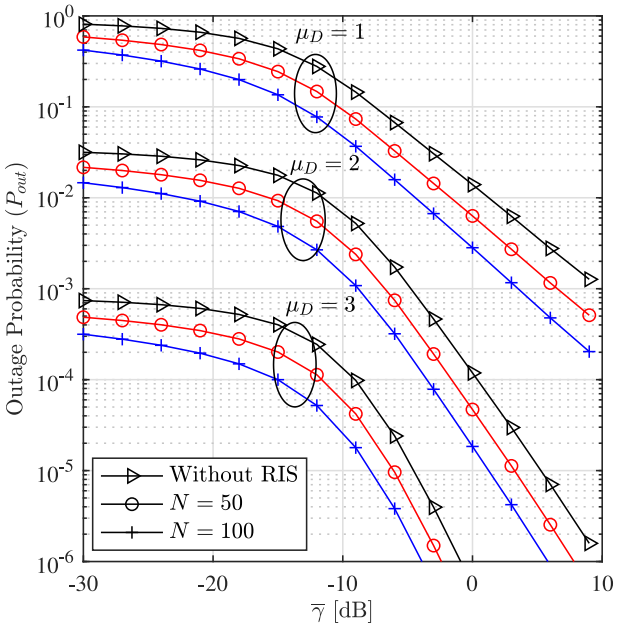

FIGURE 8. The outage probability for various values of μ_D and N where $\omega_R = \omega_D = 20$, $\mu_R = 5$, $\kappa_R = 1$, $\kappa_D = 3$, and $\gamma_{out} = 0$ dB.

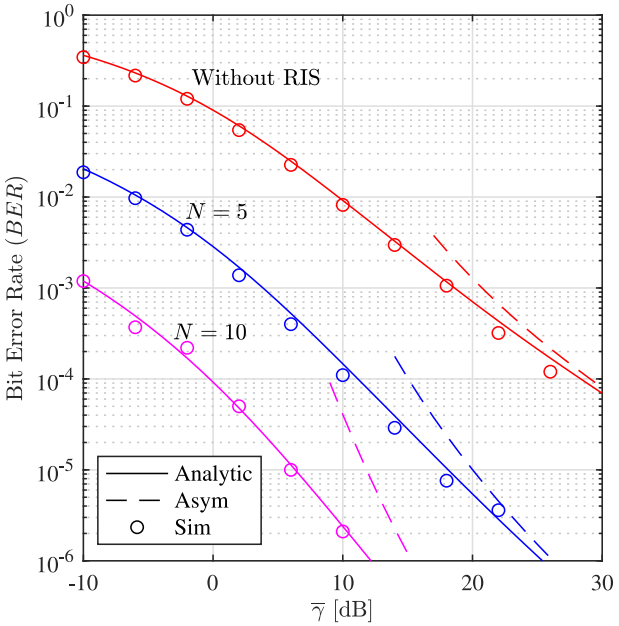

FIGURE 9. The impact of the number of reflecting elements N on the BER, $\omega_R = 4$, $\omega_D = 1$, $\mu_R = \mu_D = 1$, and $\kappa_R = \kappa_D = 1$.

values of κ_D and N on the outage probability. The results are obtained for $\kappa_R = 1$, $\mu_R = 4$, and $\mu_D = 2$. The shadowing parameter between BS-RIS and RIS-UE links is $\omega_R = 15$.

According to physical model, the ω parameter represents the level of fluctuation due to shadowing in the dominant component and the κ parameter indicates the ratio between the dominant components and the scattered waves. For large κ values, more power is present in the dominant component with respect to the scattered waves, while for large ω, the power of the dominant component is more stable and therefore there is less shadowing. Therefore, for high values of ω_D, it can be observed that the impact of κ_D becomes more tangible where P_{out} decreases by increasing κ_D. Moreover, as can be noted from the table, the P_{out} improves by improving κ_D and ω_D parameters. In addition to, it can be noted that ω_D also limits the impact of N, where increasing the value of N from 10 to 50 reduced P_{out} only by a factor of 10^2, while the improvement for the same scenario is much more significant for $\omega_D = 15$, i.e., weak shadowing.

TABLE 5. P_{out} for various κ_D and ω_D at BS-UE link, $\omega_R = 15$, $\mu_R = 4$, $\mu_D = 2$, and $\kappa_R = 1$, $\bar{\gamma} = 0$ dB, $\gamma_{out} = -20$ dB.

		ω_D			
N	κ_D	3	5	10	15
No RIS	1	0.77	0.56	0.39	0.34
	3	0.44	0.20	0.06	0.03
	5	0.31	0.10	0.01	0.005
	7	0.24	0.06	0.004	9.8×10^{-4}
10	1	0.34	0.25	0.17	0.15
	3	0.20	0.09	0.03	0.02
	5	0.14	0.04	0.006	0.002
	7	0.11	0.03	0.002	4.2×10^{-4}
20	1	0.15	0.11	0.07	0.06
	3	0.08	0.04	0.01	0.006
	5	0.06	0.02	0.002	9.1×10^{-4}
	7	0.05	0.01	7.3×10^{-4}	1.7×10^{-4}
30	1	0.06	0.04	0.03	0.03
	3	0.04	0.02	0.005	0.003
	5	0.03	0.007	9.9×10^{-4}	3.7×10^{-4}
	7	0.02	0.004	2.9×10^{-4}	7.0×10^{-4}
50	1	0.009	0.007	0.005	0.004
	3	0.006	0.002	6.9×10^{-4}	4.1×10^{-4}
	5	0.004	0.001	1.5×10^{-4}	5.6×10^{-5}
	7	0.003	6.1×10^{-4}	4.4×10^{-4}	1.04×10^{-5}

Fig. 9 shows the effect of changing the number of reflecting elements N on the BER. The exact (56) and asymptotic (59) BERs are included and compared to the Monte Carlo simulation results. The figure shows that the analytical and simulation results match very well, even for the case of $N = 5$, and $N = 10$. The BER improvement gained by using RIS seems to be significant, even when for small values of N such as $N = 5$. The asymptotic BER approaches the exact when the exact BER becomes roughly linear. For the case of no RIS and $N = 5$, the curves converge for $\bar{\gamma} \gtrsim 30$ dB, while for the case of $N = 5$ they converge for $\bar{\gamma} \gtrsim 25$ dB.

Fig. 10 evaluates the impact of the path loss exponent at RIS link (α_R) on the BER using (56). As can be noted from the figure, the BER achieved by the RIS increases by increasing α_R, and ultimately approaches the BER of the direct link regardless of the value of N. Such performance is obtained because increasing α_R causes severe signal attenuation, and hence, the signal reflected by the RIS becomes extremely weak. However, when α_R is small, a significant performance gain can be achieved by increasing N.

Fig. 11 demonstrates the advantage of using RIS-aided transmission over the direct link. Therefore, the figure illustrates the effect of increasing the distance between the RIS and UE (d_g) on P_{out}. In particular, the graph provides a

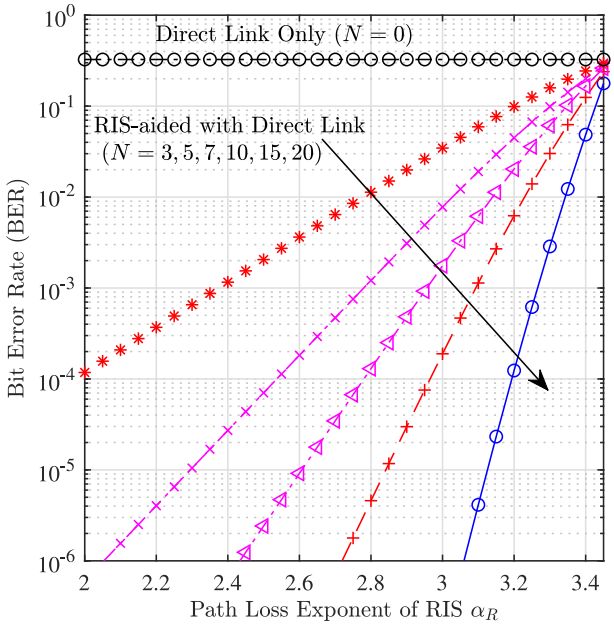

FIGURE 10. The impact of the path loss exponent (α_R) on the bit error rate (BER) where $\bar{\gamma} = 0$ dB, $\alpha_D = 3.5$, $\omega_R = 3$, $\omega_D = 4$, $\mu_R = 1$, $\mu_D = 3$, and $\kappa_R = \kappa_D = 1$.

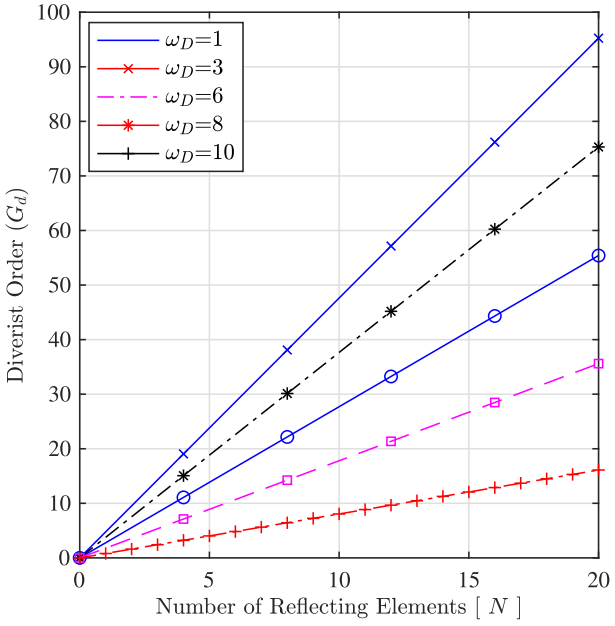

FIGURE 12. Variation in diversity order with respect to number of reflecting elements N where $\omega_R = \omega_D$, and $\mu_R = \mu_R = 1$ and $\kappa_R = \kappa_D = 1$.

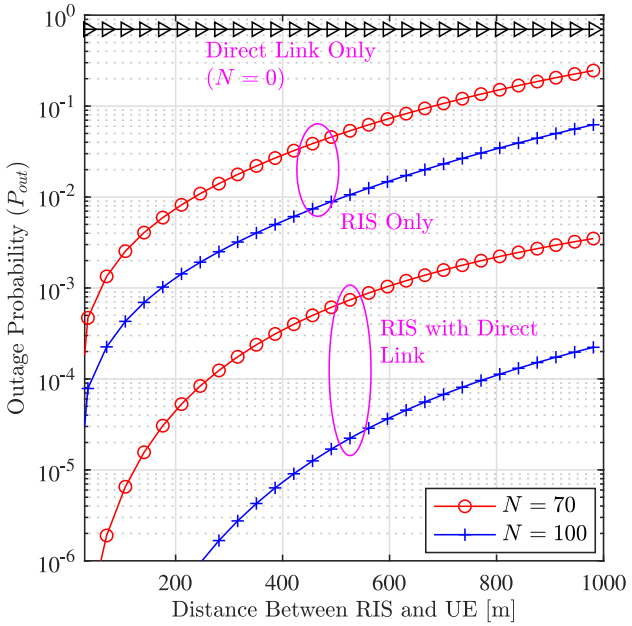

FIGURE 11. The impact of the distance between RIS and UE on outage probability (P_{out}): $\bar{\gamma} = -20$ dB, $\gamma_{out} = 0$ dB, $\omega_R = \omega_D = 5$, $\mu_R = \mu_D = 2$ and $\kappa_R = \kappa_D = 1$.

comparative analysis of three transmission schemes, which are the direct transmission only, RIS without direct transmission, and RIS transmission with a direct link. It can be noted that if the direct link is available, it is beneficial to combine both signals, notably when N increases. Moreover, it is generally difficult for the direct path alone to achieve reliable P_{out} when the outage threshold P_{out} is high. Therefore, the location of the RIS should be optimized by taking into consideration the possibility of exploiting the direct and reflected links to minimize the outage and BER.

Fig. 12 presents the diversity order of the system versus the number of reflecting elements N for various values of ω_D. Results indicate that ω_D has a significant impact on the diversity order for high values of N. When $\omega_D \gg 1$, all the reflected links have generally strong signals, and thus the diversity gained by using the RIS is limited. For low values of ω_D, the channel variations increase significantly, which increases the diversity order achieved by using the RIS.

V. CONCLUSION AND FUTURE WORK

In this paper, we developed a new analytical framework to investigate the end-to-end SNR, outage probability, and BER performance of RIS-assisted wireless communications systems over the generalized κ-μ shadowed-fading channels. Novel accurate closed-form expressions for the PDF, CDF of end-to-end SNR have been derived. Moreover, closed-form expressions have been derived for the outage and BER, which provided near-exact results. The asymptotic outage and BER are also derived to provide more insights into the achievable diversity order. The derived expressions were used to holistically study the performance of RIS systems in the presence of a direct link between the BS and UE. The results show that the direct path can significantly affect the RIS system performance, and hence, should be taken into consideration during the system's planning and design stages. Monte Carlo simulation was used to validate all the derived expressions.

In addition to providing an informative evaluation of the impact of having a direct link in RIS systems, this work also triggers several other key research problems. For example, the impact of imperfect phase estimation and compensation

can be included. In such cases, the gain obtained by the RIS will be reduced and the impact of the direct link becomes more significant. The system performance with multiple-input multiple-output (MIMO) antenna configuration would be interesting. Another interesting problem is the case where the direct link is not taken into consideration in the phase compensation process. Therefore, the direct link becomes a strong source of interference.

Our future work will focus on using the derived PDF of the SNR to evaluate the ergodic capacity of the system and evaluate the impact of the direct link for various channel conditions.

APPENDIX
PROOF OF PROPOSITION 2

The PDF of κ-μ shadowed distribution is expressed as

$$f_X(x) = \sum_{i=0}^{M} \frac{2C_i x^{2m_i-1}}{\Gamma(m_i)\Omega_i^{m_i}} \mathrm{e}^{-\frac{x^2}{\Omega_i}} \tag{62}$$

by using [77, eq. (2.2.1.7)], the Laplace transform of RV X can be written as

$$\begin{aligned} f_X(s) &= \sum_{i=0}^{M} \frac{2C_i}{\Gamma(m_i)\Omega_i^{m_i}} \mathcal{L}\left[x^{2m_i-1}\mathrm{e}^{-\frac{x^2}{\Omega_i}}\right] \\ &= \sum_{i=0}^{M} \frac{\sqrt{\pi}C_i}{\Gamma(m_i)\Omega_i^{m_i-\frac{1}{2}}}(-1)^{2m_i-1} \\ &\quad \times \frac{d^{2m_i-1}}{ds^{2m_i-1}}\left(\mathrm{erfc}\left(\sqrt{\frac{\Omega_i s^2}{4}}\right)\mathrm{e}^{\frac{\Omega_i s^2}{4}}\right). \end{aligned} \tag{63}$$

The complementary error function and error function have the relation

$$\mathrm{erfc}(x) = 1 - \mathrm{erf}(x) \tag{64}$$

where the error function can be approximated using [51, eq. (7.1.26)],

$$\begin{aligned} \mathrm{erf}\left(\frac{\sqrt{\Omega_i}s}{2}\right) &= 1 - \left(a_1 t + a_2 t^2 + a_3 t^3 + a_4 t^4 + a_5 t^5\right) \\ &\quad \times \mathrm{e}^{-\frac{\Omega_i s^2}{4}} + \epsilon\left(\frac{\sqrt{\Omega_i}s}{2}\right) \end{aligned} \tag{65}$$

where $t = \frac{1}{1+\Delta s}$, $|\epsilon(x)| \leq 1.5\times10^{-7}$. $a_1 = 0.25482959$, $a_2 = -0.284496736$, $a_3 = 1.421413741$, $a_4 = -1.453152027$, and $a_5 = 1.061405429$. By substituting (65) in (64) and substituting the result in (63), then the Laplace transform of X becomes

$$\begin{aligned} f_X(s) &= \sum_{i=0}^{M} \frac{\sqrt{\pi}C_i}{\Gamma(m_i)\Omega_i^{m_i-\frac{1}{2}}} \\ &\quad \times \frac{d^{2m_i-1}}{ds^{2m_i-1}}\left(a_1 t + a_2 t^2 + a_3 t^3 + a_4 t^4 + a_5 t^5\right) \\ &= \sum_{i=0}^{M}\sum_{\nu=1}^{5} \frac{\sqrt{\pi}C_i}{\Gamma(m_i)\Omega_i^{m_i-\frac{1}{2}}} \frac{d^{2m_i-1}}{ds^{2m_i-1}}\left(\frac{a_\nu}{(1+\Delta s)^\nu}\right). \end{aligned} \tag{66}$$

By using

$$\begin{aligned} &\frac{d^{2m_i-1}}{ds^{2m_i-1}}\left(\frac{1}{(1+\Delta s)^\nu}\right) \\ &\quad = \frac{(-1)^{2m_i-1}(2m_i+\nu-1)!\Delta^{2m_i-1}}{(\nu-1)!(1+\Delta s)^{2m_i-1+\nu}} \end{aligned}$$

and applying the inverse Laplace transform

$$\begin{aligned} \mathcal{L}^{-1}\left(\frac{1}{(1+\Delta s)^{2m_i-1+\nu}}\right) &= \frac{1}{\Delta\Gamma(2m_i+\nu-1)} \\ &\quad \times \left(\frac{1}{\Delta}\right)^{2m_i+\nu-2} x^{2m_i+\nu-2}\mathrm{e}^{-\frac{x}{\Delta}} \end{aligned} \tag{67}$$

the PDF in (24) can be obtained.

REFERENCES

[1] A. Al-Rimawi, J. Siam, A. Abdo, and D. Dardari, "Performance analysis of dynamic downlink PPP cellular networks over generalized fading channels with MRC diversity," *IEEE Access*, vol. 9, pp. 39019–39027, 2021.

[2] A. Al-Rimawi, L. Ibrahim, and W. Ajib, "Achievable rate of multi-cell downlink massive MIMO systems with D2D underly," in *Proc. IEEE 91st Veh. Technol. Conf. (VTC-Spring)*, 2020, pp. 1–5.

[3] "Ericsson mobility report, Q2 update, August 2021," Ericsson, Stockholm, Sweden, Rep., 2021. [Online]. Available: https://www.ericsson.com/en/mobility-report

[4] "Cisco annual Internet report (2018–2023)," Cisco, San Jose, CA, USA, Rep., 2020. [Online]. Available: https://www.cisco.com/c/en/us/solutions/collateral/executive-perspectives/annual-internet-report/white-paper-c11-741490.pdf

[5] A. Al-Rimawi and D. Dardari, "Characterization of link lifetime in the presence of random blocking objects," in *Proc. IEEE Int. Conf. Commun. (ICC)*, 2017, pp. 1–6.

[6] E. Basar, M. Di Renzo, J. De Rosny, M. Debbah, M.-S. Alouini, and R. Zhang, "Wireless communications through reconfigurable intelligent surfaces," *IEEE Access*, vol. 7, pp. 116753–116773, 2019.

[7] C. Liaskos, S. Nie, A. Tsioliaridou, A. Pitsillides, S. Ioannidis, and I. Akyildiz, "A new wireless communication paradigm through software-controlled metasurfaces," *IEEE Commun. Mag.*, vol. 56, no. 9, pp. 162–169, Sep. 2018.

[8] T. N. Nguyen, N. N. Thang, B. C. Nguyen, T. M. Hoang, and P. T. Tran, "Intelligent-reflecting-surface-aided bidirectional full-duplex communication system with imperfect self-interference cancellation and hardware impairments," *IEEE Syst. J.*, early access, Apr. 29, 2022, doi: 10.1109/JSYST.2022.3167514.

[9] X. Xie, H. Tang, H. Yang, Q. Huang, and D. Pu, "Intelligent reflecting surface assisted wireless information and power transfer with X-duplex for 6G networks," *IEEE Syst. J.*, early access, Nov. 4, 2021, doi: 10.1109/JSYST.2021.3120299.

[10] Z.-M. Jiang et al., "Intelligent reflecting surface aided dual-function radar and communication system," *IEEE Syst. J.*, vol. 16, no. 1, pp. 475–486, Mar. 2022.

[11] A.-A. A. Boulogeorgos and A. Alexiou, "Performance analysis of reconfigurable intelligent surface-assisted wireless systems and comparison with relaying," *IEEE Access*, vol. 8, pp. 94463–94483, 2020.

[12] M. Di Renzo et al., "Reconfigurable intelligent surfaces vs. relaying: Differences, similarities, and performance comparison," *IEEE Open J. Commun. Soc.*, vol. 1, pp. 798–807, 2020.

[13] "5G; study on channel model for frequencies from 0.5 to 100 GHz," ETSI, Sophia Antipolis, France, ETSI Rep. TR 138 901 V17.0.0, Apr. 2022. [Online]. Available: https://www.etsi.org/deliver/etsi_tr/138900_138999/138901/17.00.00_60/tr_138901v170000p.pdf

[14] M. Mirahmadi, A. Al-Dweik, and A. Shami, "Interference modeling and performance evaluation of heterogeneous cellular networks," *IEEE Trans. Commun.*, vol. 62, no. 6, pp. 2132–2144, Jun. 2014.

[15] W. Khawaja, I. Guvenc, D. W. Matolak, U.-C. Fiebig, and N. Schneckenburger, "A survey of air-to-ground propagation channel modeling for unmanned aerial vehicles," *IEEE Commun. Surveys Tuts.*, vol. 21, no. 3, pp. 2361–2391, 3rd Quart., 2019.

[16] S. K. Yoo et al., "The $\kappa-\mu$ / inverse Gamma and $\eta-\mu$ / inverse gamma composite fading models: Fundamental statistics and empirical validation," *IEEE Trans. Commun.*, vol. 69, no. 8, pp. 5514–5530, Aug. 2021.

[17] M.-J. Ho and G. Stuber, "Co-channel interference of microcellular systems on shadowed Nakagami fading channels," in *Proc. IEEE 43rd Veh. Technol. Conf.*, 1993, pp. 568–571.

[18] A. Abdi and M. Kaveh, "K Distribution: An appropriate substitute for Rayleigh-Lognormal distribution in fading-shadowing wireless channels," *Electron. Lett.*, vol. 34, pp. 851–852, Apr. 1998.

[19] J. F. Paris, "Statistical characterization of $\kappa-\mu$ shadowed fading," *IEEE Trans. Veh. Technol.*, vol. 63, no. 2, pp. 518–526, Feb. 2014.

[20] A. Abdi, W. C. Lau, M.-S. Alouini, and M. Kaveh, "A new simple model for land mobile satellite channels: First-and second-order statistics," *IEEE Trans. Wireless Commun.*, vol. 2, no. 3, pp. 519–528, May 2003.

[21] D. Tyrovolas, S. A. Tegos, E. C. Dimitriadou-Panidou, P. D. Diamantoulakis, C. K. Liaskos, and G. K. Karagiannidis, "Performance analysis of cascaded reconfigurable intelligent surface networks," *IEEE Wireless Commun. Lett.*, vol. 11, no. 9, pp. 1855–1859, Sep. 2022.

[22] P. Xu, G. Chen, Z. Yang, and M. D. Renzo, "Reconfigurable intelligent surfaces-assisted communications with discrete phase shifts: How many quantization levels are required to achieve full diversity?" *IEEE Wireless Commun. Lett.*, vol. 10, no. 2, pp. 358–362, Feb. 2021.

[23] T. Wang, G. Chen, J. P. Coon, and M.-A. Badiu, "Chernoff bound and saddlepoint approximation for outage probability in IRS-assisted wireless systems," in *Proc. IEEE Globecom Workshops (GC Wkshps)*, 2021, pp. 1–5.

[24] I. Trigui, W. Ajib, W.-P. Zhu, and M. D. Renzo, "Performance evaluation and diversity analysis of RIS-assisted communications over generalized fading channels in the presence of phase noise," *IEEE Open J. Commun. Soc.*, vol. 3, pp. 593–607, 2022.

[25] N. A. Kamaruddin, A. Mahmud, M. Y. B. Alias, A. A. Aziz, and S. Yaakob, "Performance evaluation of reconfigurable intelligent surface against distributed antenna system at the cell edge," *Electronics*, vol. 11, no. 15, p. 2376, 2022. [Online]. Available: https://www.mdpi.com/2079-9292/11/15/2376

[26] L. Yang, Y. Yang, D. B. D. Costa, and I. Trigui, "Outage probability and capacity scaling law of multiple RIS-aided networks," *IEEE Wireless Commun. Lett.*, vol. 10, no. 2, pp. 256–260, Feb. 2021.

[27] M. H. N. Shaikh, V. A. Bohara, A. Srivastava, and G. Ghatak, "On the performance of RIS-aided NOMA system with non-ideal transceiver over Nakagami-m fading," in *Proc. IEEE Wireless Commun. Netw. Conf. (WCNC)*, 2022, pp. 1737–1742.

[28] K. Odeyemi, P. Owolawi, and O. Olakanmi, "Reconfigurable intelligent surface in wireless-powered interference-limited communication networks," *Symmetry*, vol. 13, no. 6, p. 960, 2021. [Online]. Available: https://www.mdpi.com/2073-8994/13/6/960

[29] D. Kudathanthirige, D. Gunasinghe, and G. Amarasuriya, "Performance analysis of intelligent reflective surfaces for wireless communication," in *Proc. IEEE Int. Conf. Commun. (ICC)*, 2020, pp. 1–6.

[30] S. Atapattu, R. Fan, P. Dharmawansa, G. Wang, J. Evans, and T. A. Tsiftsis, "Reconfigurable intelligent surface assisted two–way communications: Performance analysis and optimization," *IEEE Trans. Commun.*, vol. 68, no. 10, pp. 6552–6567, Oct. 2020.

[31] M.-A. Badiu and J. P. Coon, "Communication through a large reflecting surface with phase errors," *IEEE Commun. Lett.*, vol. 9, no. 2, pp. 184–188, Feb. 2020.

[32] I. Trigui, W. Ajib, and W.-P. Zhu, "A comprehensive study of reconfigurable intelligent surfaces in generalized fading," 2020, *arXiv:2004.02922*.

[33] E. BjÖrnson and L. Sanguinetti, "Demystifying the power scaling law of intelligent reflecting surfaces and metasurfaces," in *Proc. IEEE 8th Int. Workshop Comput. Adv. Multi-Sens. Adapt. Process. (CAMSAP)*, 2019, pp. 549–553.

[34] M. Jung, W. Saad, Y. Jang, G. Kong, and S. Choi, "Performance analysis of large intelligent surfaces (LISs): Asymptotic data rate and channel hardening effects," *IEEE Trans. Wireless Commun.*, vol. 19, no. 3, pp. 2052–2065, Mar. 2020.

[35] D. Li, "Ergodic capacity of intelligent reflecting surface-assisted communication systems with phase errors," *IEEE Commun. Lett.*, vol. 24, no. 8, pp. 1646–1650, Aug. 2020.

[36] T. Wang, G. Chen, J. P. Coon, and M.-A. Badiu, "Study of intelligent reflective surface assisted communications with one-bit phase adjustments," in *Proc. IEEE Global Commun. Conf. (GLOBECOM)*, 2020, pp. 1–6.

[37] Q. Tao, J. Wang, and C. Zhong, "Performance analysis of intelligent reflecting surface aided communication systems," *IEEE Commun. Lett.*, vol. 24, no. 11, pp. 2464–2468, Nov. 2020.

[38] B. Tahir, S. Schwarz, and M. Rupp, "Analysis of uplink IRS-assisted NOMA under Nakagami-*m* fading via moments matching," *IEEE Commun. Lett.*, vol. 10, no. 3, pp. 624–628, Mar. 2021.

[39] V.-D. Phan et al., "Performance of cooperative communication system with multiple reconfigurable intelligent surfaces over Nakagami-m fading channels," *IEEE Access*, vol. 10, pp. 9806–9816, 2022.

[40] B. C. Nguyen, L. T. Dung, T. M. Hoang, N. V. Vinh, and G. T. Luu, "On performance of multi-RIS assisted multi-user nonorthogonal multiple access system over Nakagami-m fading channels," *Comput. Commun.*, vol. 197, pp. 294–305, Nov. 2022. [Online]. Available: https://www.sciencedirect.com/science/article/pii/S0140366422004339

[41] O. Waqar, "Performance analysis for IRS-aided communication systems with composite fading/shadowing direct link and discrete phase shifts," *Trans. Emerg. Telecommun. Technol.*, vol. 32, no. 10, p. e4320, 2021.

[42] H. Ibrahim, H. Tabassum, and U. T. Nguyen, "Exact coverage analysis of intelligent reflecting surfaces with nakagami-*m* channels," *IEEE Trans. Veh. Technol.*, vol. 70, no. 1, pp. 1072–1076, Jan. 2021.

[43] J. Lyu and R. Zhang, "Spatial throughput characterization for intelligent reflecting surface aided multiuser system," *IEEE Wireless Commun. Lett.*, vol. 9, no. 6, pp. 834–838, Jun. 2020.

[44] Q. Wu, S. Zhang, B. Zheng, C. You, and R. Zhang, "Intelligent reflecting surface-aided wireless communications: A tutorial," *IEEE Trans. Commun.*, vol. 69, no. 5, pp. 3313–3351, May 2021.

[45] A. Al-Rimawi and D. Dardari, "Analytical characterization of device-to-device and cellular networks coexistence," *IEEE Trans. Wireless Commun.*, vol. 16, no. 8, pp. 5537–5548, Aug. 2017.

[46] L. Moreno-Pozas, F. J. Lopez-Martinez, J. F. Paris, and E. Martos-Naya, "The $\kappa-\mu$ shadowed fading model: Unifying the $\kappa-\mu$ and $\eta-\mu$ distributions," *IEEE Trans. Veh. Technol.*, vol. 65, no. 12, pp. 9630–9641, Dec. 2016.

[47] E. Basar, "Transmission through large intelligent surfaces: A new frontier in wireless communications," in *Proc. Eur. Conf. Netw. Commun. (EuCNC)*, 2019, pp. 112–117.

[48] M. Jung, W. Saad, Y. Jang, G. Kong, and S. Choi, "Reliability analysis of large intelligent surfaces (LISs): Rate distribution and outage probability," *IEEE Wireless Commun. Lett.*, vol. 8, no. 6, pp. 1662–1666, Dec. 2019.

[49] I. S. Gradshteyn and I. M. Ryzhik, *Table of Integrals, Series, and Products*, 7th ed. Amsterdam, The Netherlands: Elsevier, 2007.

[50] M. Abramowitz and I. A. Stegun, *Handbook of Mathematical Functions with Formulas, Graphs, and Mathematical Tables*, 9th ed. New York, NY, USA: Dover, 1964.

[51] H. Exton, *Multiple Hypergeometric Functions and Applications* (Mathematics & Its Applications), L. J. Slater, Ed. Chichester, U.K.: Ellis Horwood Ltd., 1976.

[52] W. Tang et al., "Wireless communications with reconfigurable intelligent surface: Path loss modeling and experimental measurement," *IEEE Trans. Wireless Commun.*, vol. 20, no. 1, pp. 421–439, Jan. 2021.

[53] M. Jian et al., "Reconfigurable intelligent surfaces for wireless communications: Overview of hardware designs, channel models, and estimation techniques," *Intell. Converg. Netw.*, vol. 3, no. 1, pp. 1–32, 2022.

[54] T. V. Chien et al., "Outage probability analysis of IRS-assisted systems under spatially correlated channels," *IEEE Wireless Commun. Lett.*, vol. 10, no. 8, pp. 1815–1819, Aug. 2021.

[55] C. Psomas and I. Krikidis, "SWIPT with intelligent reflecting surfaces under spatial correlation," *IEEE Wireless Commun. Lett.*, vol. 10, no. 9, pp. 1924–1928, Sep. 2021.

[56] T. Bao, H. Wang, H.-C. Yang, W.-J. Wang, and M. O. Hasna, "Performance analysis of RIS-aided communication systems over the sum of cascaded Rician fading with imperfect CSI," in *Proc. IEEE Wireless Commun. Netw. Conf. (WCNC)*, 2022, pp. 399–404.

[57] A. Zappone, M. Di Renzo, F. Shams, X. Qian, and M. Debbah, "Overhead-aware design of reconfigurable intelligent surfaces in smart radio environments," *IEEE Trans. Wireless Commun.*, vol. 20, no. 1, pp. 126–141, Jan. 2021.

[58] J. Praia, J. P. Pavia, N. Souto, and M. Ribeiro, "Phase shift optimization algorithm for achievable rate maximization in reconfigurable intelligent surface-assisted THz communications," *Electronics*, vol. 11, no. 1, p. 18, 2022. [Online]. Available: https://www.mdpi.com/2079-9292/11/1/18

[59] Q. Wu and R. Zhang, "Towards smart and reconfigurable environment: Intelligent reflecting surface aided wireless network," *IEEE Commun. Mag.*, vol. 58, no. 1, pp. 106–112, Jan. 2020.

[60] T. Shafique, H. Tabassum, and E. Hossain, "Optimization of wireless relaying with flexible UAV-borne reflecting surfaces," *IEEE Trans. Commun.*, vol. 69, no. 1, pp. 309–325, Jan. 2021.

[61] M. Al-Jarrah, A. Al-Dweik, E. Alsusa, Y. Iraqi, and M.-S. Alouini, "On the performance of IRS-assisted multi-layer UAV communications with imperfect phase compensation," *IEEE Trans. Commun.*, vol. 69, no. 12, pp. 8551–8568, Dec. 2021.

[62] M. A. Al-Jarrah, E. Alsusa, A. Al-Dweik, and M.-S. Alouini, "Performance analysis of wireless mesh backhauling using intelligent reflecting surfaces," *IEEE Trans. Wireless Commun.*, vol. 20, no. 6, pp. 3597–3610, Jun. 2021.

[63] M. Al-Jarrah, E. Alsusa, A. Al-Dweik, and D. K. C. So, "Capacity analysis of IRS-based UAV communications with imperfect phase compensation," *IEEE Wireless Commun. Lett.*, vol. 10, no. 7, pp. 1479–1483, Jul. 2021.

[64] E. Björnson, O. Özdogan, and E. G. Larsson, "Intelligent reflecting surface versus decode-and-forward: How large surfaces are needed to beat relaying?" *IEEE Wireless Commun. Lett.*, vol. 9, no. 2, pp. 244–248, Feb. 2020.

[65] Q. Wu and R. Zhang, "Intelligent reflecting surface enhanced wireless network via joint active and passive beamforming," *IEEE Trans. Wireless Commun.*, vol. 18, no. 11, pp. 5394–5409, Nov. 2019.

[66] C. Huang, A. Zappone, G. C. Alexandropoulos, M. Debbah, and C. Yuen, "Reconfigurable intelligent surfaces for energy efficiency in wireless communication," *IEEE Trans. Wireless Commun.*, vol. 18, no. 8, pp. 4157–4170, Aug. 2019.

[67] Z.-Q. He and X. Yuan, "Cascaded channel estimation for large intelligent metasurface assisted massive MIMO," *IEEE Wireless Commun. Lett.*, vol. 9, no. 2, pp. 210–214, Feb. 2020.

[68] F. J. Lopez-Martinez, J. F. Paris, and J. M. Romero-Jerez, "The $\kappa-\mu$ shadowed fading model with integer fading parameters," *IEEE Trans. Veh. Technol.*, vol. 66, no. 9, pp. 7653–7662, Sep. 2017.

[69] S. L. Cotton, "Human body shadowing in cellular device-to-device communications: Channel modeling using the shadowed $\kappa-\mu$ fading model," *IEEE J. Sel. Areas Commun.*, vol. 33, no. 1, pp. 111–119, Jan. 2015.

[70] F. J. Cañete et al., "Measurement and modeling of narrowband channels for ultrasonic underwater communications," *Sensors*, vol. 16, p. 256, Feb. 2016.

[71] S. L. Cotton, "Shadowed fading in body-to-body communications channels in an outdoor environment at 2.45 GHz," in *Proc. IEEE-APS Topical Conf. Antennas Propag. Wireless Commun. (APWC)*, 2014, pp. 249–252.

[72] F. J. Lopez-Martinez, L. Moreno-Pozas, U. Fernandez-Plazaola, J. F. Paris, E. Martos-Naya, and J. M. Romero-Jerez, "A tractable line-of-sight product channel model: Application to wireless powered communications," in *Proc. 15th Int. Symp. Wireless Commun. Syst. (ISWCS)*, 2018, pp. 1–5.

[73] A. Erdelyi, W. Magnus, F. Oberhettinger, and F. G. Tricomi, *Tables of Integral Transforms. Vol. I: Based, in Part, on Notes Left by Harry Batemann*. New York, NY, USA: McGraw-Hill, 1954.

[74] E. Martos-Naya, J. M. Romero-Jerez, F. J. LÓpez-Martínez, and J. F. Paris, *A MATLAB Program for the Computation of the Confluent Hypergeometric Function* Φ_2, MATLAB, Natick, MA, USA, 2016.

[75] M. A. Al-Jarrah, K.-H. Park, A. Al-Dweik, and M.-S. Alouini, "Error rate analysis of amplitude-coherent detection over Rician fading channels with receiver diversity," *IEEE Trans. Wireless Commun.*, vol. 19, no. 1, pp. 134–147, Jan. 2020.

[76] Z. Wang and G. B. Giannakis, "A simple and general parameterization quantifying performance in fading channels," *IEEE Trans. Commun.*, vol. 51, no. 8, pp. 1389–1398, Aug. 2003.

[77] A. P. Prudnikov, Y. A. Brychkov, and O. I. Marichev, *Integrals and Series: Volume 2, Special Functions*. New York, NY, USA: Gordon Breach Sci. Publ., 1992.

ASHRAF AL-RIMAWI (Member, IEEE) received the B.S. degree in electrical engineering from Birzeit University, Palestine, in 2008, the master's degree in wireless communication from the Jordan University of Science and Technology in 2012, and the Ph.D. degree in wireless communication from Bologna University in 2017. During his Ph.D. period, he participated in the H2020 Xcycle Project, Italy. He was a Teaching and Research Assistant with Al-Quds University, Duisburg-Essen University, Jordan University of Science and Technology, and Bologna University. He is a member of Palestine Communication and Informatics Society and has been a Lecturer with the Department of Electrical and Computer Engineering, Birzeit University, since 2012, where he is currently an Assistant Professor. He has published several journal and conference papers in the IEEE TRANSACTION WIRELESS COMMUNICATION and strong congress conferences, such as VTC and ICC. His research is on the theory and development of wireless communication systems, mathematical modeling and analysis of emerging wireless communication architectures, leading to innovative and/or theoretically optimal new communication techniques. He is chosen as one of the Reviewers in the IEEE TRANSACTION WIRELESS COMMUNICATION, IEEE WIRELESS COMMUNICATION LETTER, and several conferences.

ARAFAT AL-DWEIK (Senior Member, IEEE) received the M.S. degree *(summa cum laude)* and the Ph.D. degree *(magna cum laude)* in electrical engineering from Cleveland State University, Cleveland, OH, USA, in 1998 and 2001, respectively.

He is currently with the Department of Electrical Engineering and Computer Science, Khalifa University, Abu Dhabi, UAE. He also worked with Efficient Channel Coding, Inc., Cleveland, OH, USA, Department of Information Technology, Arab American University, Jenin, Palestine, and the University of Guelph, Guelph, ON, Canada. He is a Visiting Research Fellow with the School of Electrical, Electronic, and Computer Engineering, Newcastle University, Newcastle upon Tyne, U.K, and a Research Professor with Western University, London, ON, Canada, and the University of Guelph, Guelph. He has extensive research experience in various areas of wireless communications that include modulation techniques, channel modeling and characterization, synchronization and channel estimation techniques, OFDM technology, error detection and correction techniques, MIMO, and resource allocation for wireless networks.

Dr. Al-Dweik was awarded the Fulbright scholarship from 1997 to 1999. He was the recipient of the Hijjawi Award for Applied Sciences in 2003, the Fulbright Alumni Development Grant in 2003 and 2005, the Dubai Award for Sustainable Transportation in 2016, and the UAE Leader-Founder Award in 2019. He serves as an Associate Editor for the IEEE TRANSACTIONS ON VEHICULAR TECHNOLOGY and the *IET Communications*. He is a Registered Professional Engineer in the Province of Ontario, Canada. He is a member of Tau Beta Pi and Eta Kappa Nu.